Research Article

Journal of Environmental Nanotechnology

Green Synthesis of *Passiflora foetida*-mediated MnO_2 Nanoparticles for Rhodamine B Photodegradation, Antioxidant Activity and Gelatin Film Reinforcement

Nidhi Sharma[1], Pramod G. Musrif[1], Manisha Raghuvanshi[1], Nitin P. Bhone[1], Mayank Choubey[2] and P. Satishkumar[3]*

[1]Department of Applied Sciences and Engineering, AISSMS Institute of Information Technology, Pune, MH, India
[2]Department of Mechanical Engineering, Faculty of Engineering and Technology, SGT University, Gurgaon, HR, India
[3]Department of Mechanical Engineering, Rathinam Technical Campus, Coimbatore, TN, India
Received: 29.07.2026 Accepted: 27.08.2026 Published: 30.09.2026
*spsatishkumar1986@gmail.com

ABSTRACT

Plant-assisted synthesis was adopted as a sustainable, uncomplicated, and economical approach for producing MnO_2 nanoparticles. *Passiflora foetida* leaf extract supplied phytochemicals that mediated the reduction of potassium permanganate and stabilised the resulting particles. UV–Vis spectroscopy, XRD, FTIR, and EDAX were employed to establish their formation, structure, surface chemistry, and elemental composition. A characteristic absorption band at approximately 285 nm supported MnO_2 formation. The XRD pattern revealed a nanocrystalline structure, with an average crystallite size of nearly 19 nm calculated using the Debye–Scherrer equation. FTIR analysis demonstrated the involvement of hydroxyl, carbonyl, and other plant-derived functional groups in particle formation and surface stabilisation, whereas EDAX confirmed manganese and oxygen as the predominant elements. Photocatalytic experiments produced a maximum Rhodamine B degradation efficiency of 97.8% at pH 7.0. Efficiency declined above the optimum dye concentration because concentrated solutions restricted light penetration and increased competition for reactive surface sites. The prepared MnO_2 nanoparticles also displayed considerable antioxidant activity, producing EC_{50} values of 31.46 ± 1.08 µg/mL and 35.18 ± 1.15 µg/mL in ABTS and DPPH assays. Mechanical testing of MnO_2-reinforced gelatin films showed that formulation S5, containing 46 mL of gelatin solution and 4 mL of MnO_2 suspension (4000 µg MnO_2), achieved the highest elastic modulus of 845 MPa and tensile strength of 71 MPa. Overall, the developed nanomaterial demonstrated promising photocatalytic, antioxidant, and film-strengthening performance for sustainable wastewater-treatment applications.

Keywords: Plant synthesis; Absorption band; Rhodamine B; Antioxidant activity; Wastewater.

1. INTRODUCTION

The rapid growth of industrialization has resulted in the continuous discharge of synthetic dyes, pharmaceutical residues, and other hazardous organic pollutants into aquatic environments, posing serious threats to ecosystems and human health. Conventional wastewater treatment technologies often suffer from incomplete pollutant removal, secondary contamination, and high operational costs. Consequently, semiconductor photocatalysis has emerged as an efficient and environmentally sustainable approach for degrading persistent organic contaminants through the generation of reactive oxygen species under light irradiation. Among various photocatalysts, manganese dioxide (MnO_2) has attracted considerable attention because of its multiple oxidation states, excellent redox characteristics, low toxicity, and cost-effective preparation. Furthermore, plant-mediated green synthesis has emerged as a low-cost and eco-friendly alternative for preparing metal oxide nanoparticles using plant-derived constituents as biological reaction media (Blessymol *et al.* 2023).

Recent studies have demonstrated remarkable progress in MnO_2-based photocatalysts for environmental remediation. A hydrothermally synthesized K-birnessite MnO_2 membrane efficiently activated peroxymonosulfate to degrade methylene blue under simulated sunlight at a 1 mL min^{-1} flow rate while maintaining catalytic activity under dark conditions (Tang *et al.* 2023). Similarly, BiOCl–MnO_2/PVA hydrogel films achieved 99% Rhodamine B degradation within 60 min and 97% ibuprofen degradation within 90 min, retaining more than 80% photocatalytic efficiency after five reuse cycles (Chiam *et al.* 2025). MnO_2–ZnO/SiO_2 nanofibrous membranes further exhibited 98.1% malachite green degradation within 15 min with a degradation rate of 0.2744 min^{-1}, demonstrating excellent catalytic efficiency and recyclability (Shi *et al.* 2023). Green-synthesized rGO–MnO_2/CuO nanocomposites also enhanced metanil yellow degradation from 87% to 96% by reducing the band gap to 2.04 eV, while simultaneously improving antibacterial performance (Jeoffrey *et al.* 2023). Likewise, PDA/MnO_2-interlayer nanofiltration membranes

maintained a flux recovery ratio above 95% with a water permeance of 24 ± 2 L m^{-2} h^{-1} bar^{-1}, illustrating the advantages of MnO_2 in self-cleaning membrane systems (Mei *et al.* 2023).

Green synthesis has further expanded the application of metal oxide nanoparticles using naturally occurring phytochemicals as reducing and stabilizing agents. *Passiflora foetida* fruit peel-mediated ZnO nanoparticles exhibited an average particle size of ~58 nm and degraded 93.25% methylene blue and 91.06% Rhodamine B within 70 min under natural sunlight (Khan *et al.* 2021). Similarly, *Camellia sinensis*-mediated $MnFe_2O_4$ nanoparticles achieved 44.5% methylene blue degradation with a reduced band gap of 1.11 eV, while improving Vigna radiata seed germination to 89.6% after wastewater treatment (Mungle *et al.* 2026). Green-synthesized CeO_2/rGO nanohybrids prepared using *Carica papaya* leaf extract possessed a 95 m^2 g^{-1} surface area, 2.91 eV band gap, and retained >95% degradation efficiency after four photocatalytic cycles (Loganathan *et al.* 2026). These findings highlight the potential of plant-derived phytochemicals to produce stable nanostructured photocatalysts with enhanced optical and catalytic properties.

Beyond wastewater remediation, MnO_2-based nanomaterials have demonstrated multifunctional properties in sensing, biomedical engineering, and polymer nanocomposites. In situ generated MnO_2 enabled highly sensitive glutathione sensing with a 57 nM detection limit and recoveries of 93.53–102.77% (Gao *et al.* 2026), while MnO_2/MWCNT nanocomposites exhibited enhanced thermal stability, specific capacitance, and antibacterial activity (Thilaga *et al.* 2025). MMP/ROS-responsive MnO_2-containing hydrogels enabled sustained drug release for hypertrophic scar treatment (Suo *et al.* 2025), whereas biodegradable polymeric systems incorporating inorganic nanomaterials have shown significant improvements in antioxidant activity, antimicrobial performance, and mechanical strength. For example, PBAT films containing tannic acid/ZnS nanohybrids exhibited 90.46% DPPH scavenging activity, 97% UV blocking, and reduced water vapor permeability by 40.9% (Niksefat *et al.* 2026), while Ag-incorporated PVA/agar/tannic acid hydrogels improved tensile strength from 9.66 to 12 MPa and fracture toughness from 16.51 to 19.5 MJ m^{-3} (Rahmani *et al.* 2025). These studies indicate that incorporating functional nanoparticles into biodegradable polymers provides a promising strategy for producing multifunctional materials with environmental and biomedical relevance.

Although green-synthesized MnO_2 nanoparticles have attracted considerable interest, the use of *Passiflora foetida* leaf extract as a natural reducing and stabilizing agent remains insufficiently explored. Moreover, previous studies have generally examined the photocatalytic, antioxidant, or polymer-reinforcing properties of MnO_2 nanoparticles independently. Consequently, limited information is available on integrating these functions within a single, sustainably synthesized MnO_2-based system.

The novelty of the present study lies in the green synthesis of multifunctional MnO_2 nanoparticles using *P. foetida* leaf extract and their systematic evaluation for three complementary applications: photocatalytic degradation of Rhodamine B, antioxidant activity through DPPH and ABTS assays, and mechanical reinforcement of biodegradable gelatin films. The study therefore connects wastewater remediation, antioxidant functionality, and sustainable packaging-material development within one nanomaterial platform. This integrated approach demonstrates the potential of *P. foetida*-mediated MnO_2 nanoparticles as environmentally sustainable materials for both water-treatment and biodegradable-film applications.

2. MATERIALS AND METHODOLOGY

2.1 Materials

Fresh *Passiflora foetida* leaves belonging to the Passifloraceae family were collected from Tamil Nadu, southern India. Analytical-grade potassium permanganate ($KMnO_4$; purity >99%; molar mass 158.03 g mol^{-1}) was procured from Star Scientific Enterprises, Erode, India. Double-distilled water with a conductivity of 1.05×10^{-6} S cm^{-1} served as the solvent throughout the experiments. Rhodamine B ($C_{28}H_{31}ClN_2O_3$), with a molar mass of 479.02 g mol^{-1}, was purchased from Star Scientific Enterprises, Erode, India. Gelatin was employed as the film-forming polymer for incorporating the prepared MnO_2 nanoparticles. Double-distilled water was used for solution preparation and washing.

2.2 Preparation of MnO_2 Nanoparticles Using *Passiflora foetida* Leaf Extract

Approximately 100 g of fresh *Passiflora foetida* leaves were collected and repeatedly rinsed with tap water, followed by distilled water to eliminate adhering soil and contaminants. The cleaned leaves were air-dried at ambient temperature (approximately 34 °C) for 10 days. Dried material, weighing approximately 35 g, was ground into a fine powder. For extract preparation, 20 g of leaf powder was dispersed in 200 mL of deionized water and heated at 65 °C for 10 min under continuous stirring. The obtained greenish-brown extract was cooled to room temperature and filtered through Whatman No. 1 filter paper with an approximate pore size of 11 µm. The filtrate was stored at 5 °C until nanoparticle synthesis.

For MnO_2 formation, 10 mL of the prepared leaf extract was gradually introduced into 100 mL of 0.01 M

potassium permanganate solution. The reaction mixture was continuously stirred at 300 rpm and 60 °C for 30 min (Panda *et al.* 2025). Its colour changed from purple to dark brownish-black, indicating reduction of permanganate ions and formation of MnO_2. The suspension was centrifuged at 15,000 rpm for 20 min, and the recovered precipitate was repeatedly washed with distilled water and ethanol to eliminate residual plant compounds. The purified product was oven-dried at 80 °C and subsequently converted into a fine MnO_2 nanoparticle powder. Synthesis conditions were optimised by varying the extract volume, reaction period, and potassium permanganate concentration.

Passiflora foetida leaf extract offers several advantages over conventional chemical reagents during the preparation of MnO_2 nanoparticles (Triadisti and Zamzani, 2023). The extract contains phenolic compounds, flavonoids, alkaloids, and other phytochemicals. These constituents facilitate the conversion of Mn(VII) in potassium permanganate into Mn(IV) oxide and help control particle aggregation through surface stabilisation. The plant extract is renewable, biodegradable, and comparatively low in toxicity. Its use minimises dependence on hazardous reducing and stabilising chemicals, thereby supporting the principles of sustainable chemistry. *Passiflora foetida* is readily available across many tropical regions. Its aqueous extraction requires uncomplicated equipment, moderate temperatures, and inexpensive processing conditions, which can reduce the overall production cost. Residual plant-derived molecules associated with the nanoparticle surface may contribute antioxidant activity and improve colloidal stability. These characteristics can enhance the functional performance of MnO_2 nanoparticles in Rhodamine B degradation and related environmental applications. Collectively, its phytochemical diversity, accessibility, low environmental impact, and multifunctional activity make *Passiflora foetida* leaf extract a suitable biological medium for the sustainable production of stable MnO_2 nanoparticles.

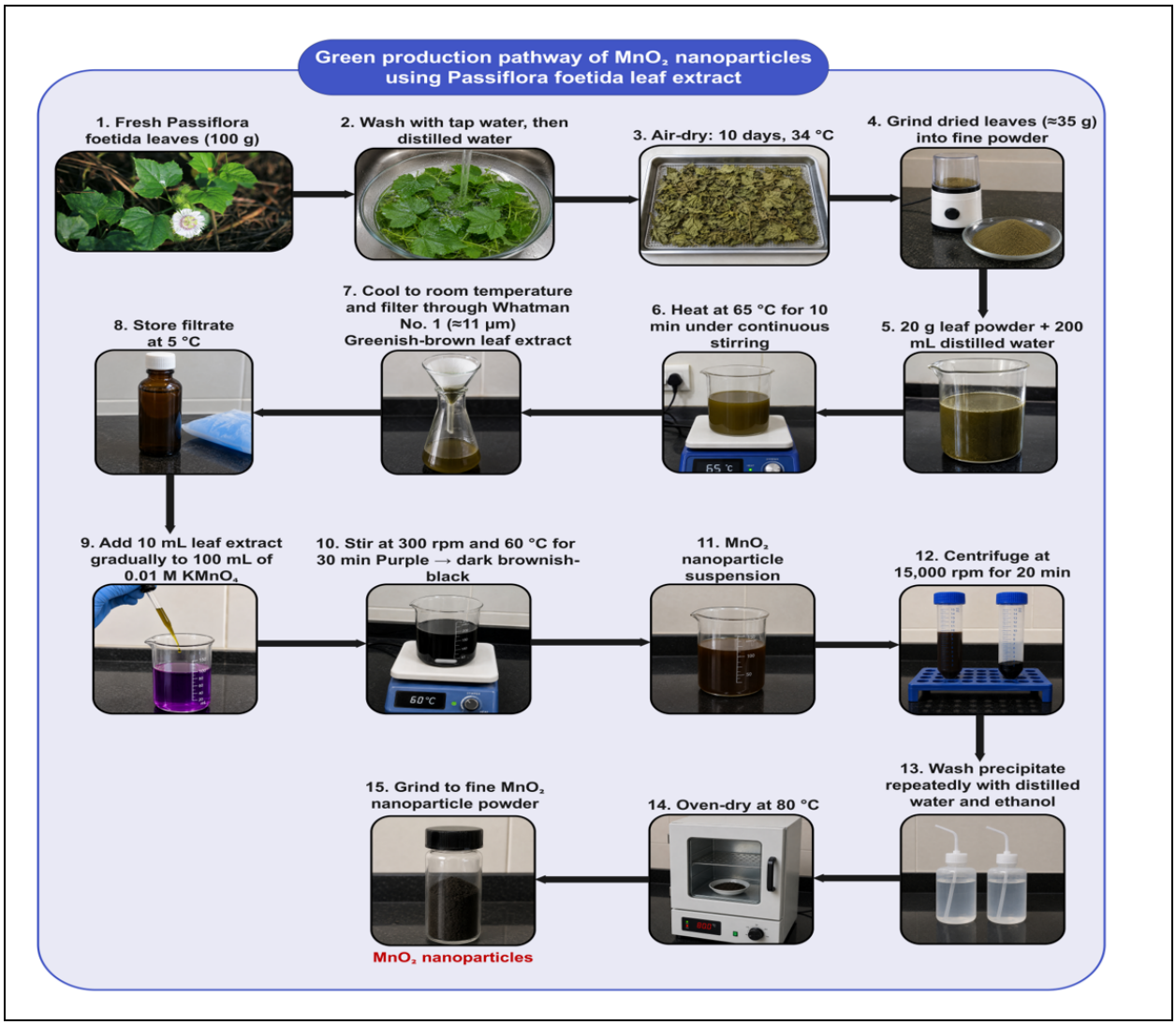

Fig. 1: Green production pathway of MnO_2 nanoparticles from potassium permanganate using *Passiflora foetida* leaf extract

2.3 Preparation of MnO_2-reinforced Gelatin Films

Gelatin–MnO_2 nanocomposite films were fabricated using the solution-casting technique. An 8% (w/v) gelatin solution were prepared in distilled water and continuously stirred at 700 rpm for 30 min at 60 °C until completely dissolved (Hakimi *et al.* 2024). A MnO_2 nanoparticle stock suspension of 1000 mg/L was separately prepared and ultrasonicated to minimise particle agglomeration. Different volumes of the MnO_2 suspension were incorporated into the gelatin solution according to the formulations listed in Table 1. The total casting volume was maintained at 50 mL for each sample. Every formulation was stirred until a homogeneous dispersion was obtained and subsequently poured into clean glass Petri dishes. The cast mixtures were cooled to room temperature and dried under ambient conditions for 2 days. Finally, dried films was carefully removed from the Petri dishes and conditioned before mechanical characterisation.

Table 1. Formulation of gelatin films containing different concentrations of MnO_2 nanoparticles

S. No.	Sample	Gelatin (mL)	MnO_2 Nanoparticles
1	S1	50	0
2	S2	49	1 mL or 1000 µg
3	S3	48	2 mL or 2000 µg
4	S4	47	3 mL or 3000 µg
5	S5	46	4 mL or 4000 µg

2.4 Characterisation and Performance Assessment of Biosynthesised MnO_2 Nanoparticles

MnO_2 nanoparticle formation from potassium permanganate and *Passiflora foetida* leaf extract was monitored using a Shimadzu UV-1900i UV–Vis (ultraviolet–visible) spectrophotometer fitted with a 1.0 cm quartz cuvette. Spectra were recorded between 200 and 800 nm. Surface functional groups associated with particle formation and stabilisation were examined using a PerkinElmer Spectrum Two FTIR Fourier-transform infrared spectrometer. Dried samples were combined with KBr, compressed into pellets, and scanned over 4000–400 cm^{-1}. The crystalline structure was investigated using a PANalytical X'Pert PRO diffractometer operated at 40 kV and 40 mA with Cu Kα radiation (λ = 1.5406 Å). Diffraction data were collected across $20° \leq 2\theta \leq 80°$ with a step size of 0.02°. Morphology and elemental composition were examined using a ZEISS Gemini field-emission scanning electron microscope connected to an energy-dispersive X-ray spectroscopy (EDS) detector (Sharmiladevi *et al.* 2024). Approximately 5.0 µL of nanoparticle suspension was placed on conductive carbon tape and vacuum-dried at 50 °C for 12 h before analysis.

Mechanical properties of the pure gelatin film (S1) and MnO_2-containing films (S2–S5) were determined using Instron 3345 universal testing machine (UTM) equipped with 5 kN load cell. Uniform film strips were prepared, and elastic modulus, tensile strength, and elongation at break were measured. Each formulation was examined three times, and mean values were reported.

Photocatalytic performance was examined through Rhodamine B degradation in a UV-assisted batch reactor. Approximately 50 mg of MnO_2 nanoparticles was dispersed in 50 mL of 3.5×10^{-5} mol/L Rhodamine B solution (Zhang *et al.* 2026). Treatment was conducted at pH 7.0 and 45 °C for 60 min under continuous stirring. Before irradiation, the suspension was kept in darkness to attain adsorption–desorption equilibrium. Two 15 W UV lamps emitting at 365 nm and providing an intensity of approximately 1 mW/cm² were used for irradiation. A corresponding suspension maintained without UV exposure served as the dark control. Residual Rhodamine B was quantified at 554 nm, and degradation efficiency was calculated using Equation (1) (Tiwari *et al.* 2025):

$$\text{Rhodamine B degradation } (\%) = \frac{A_0 - A_t}{A_0} \times 100 \quad \ldots (1)$$

2.5 Free-radical Scavenging Activity of MnO_2 Nanoparticles

Antioxidant potential of the biosynthesised MnO_2 nanoparticles was examined by ABTS [2,2'-azino-bis (3-ethylbenzothiazoline-6-sulphonic acid)]and DPPH (2,2-diphenyl-1-picrylhydrazyl) radical-scavenging assays.

For the DPPH assay, MnO_2 nanoparticle suspensions with concentrations from 10 to 100μ g/mL was individually combined with 1 mL of 0.1 M acetate buffer and 0.5 mL of a 250μM DPPH methanolic solution. Methanol was added to obtain a final reaction volume of 3 mL. Each mixture was vortexed thoroughly and incubated at 34 °C for 30 min under dark conditions. Absorbance were subsequently recorded at 517 nm by Agilent Cary 60 UV-Vis spectrophotometer. A reaction mixture without MnO_2 nanoparticles was used as the control, while ascorbic acid served as the antioxidant reference. Sample blanks without DPPH were also measured to correct for nanoparticle-related absorption and light scattering.

ABTS radical solution was created by mixing equal volumes of 2.45 mM potassium persulfate and 7 mM ABTS solutions. These were maintained in darkness at 34°C for 12 h to permit complete radical formation. Before analysis, the solution was diluted with methanol until an absorbance of 0.70 ± 0.02 was obtained at 734

nm. Different MnO_2 concentrations, ranging from 10 to 100μ g/mL, were separately introduced into 3 mL of diluted ABTS radical solution.

2,2-diphenyl-1-picrylhydrazyl (DPPH) and 2,2′-azino-bis(3-ethylbenzothiazoline-6-sulfonic acid) ABTS radical-scavenging efficiencies were calculated using Equation (2) (Revathi *et al.* 2023):

$$\text{Radical-scavenging activity (\%)} = \frac{A_C - A_S}{A_C} \times 100 \quad \ldots (2)$$

3. RESULT AND DISCUSSION

3.1 Characterisation of Biosynthesised MnO_2 Nanoparticles

3.1.1 Optimisation of *Passiflora foetida* Leaf Extraction

The aqueous extraction conditions for *Passiflora foetida* leaves were optimized by examining leaf mass, extraction temperature, and processing time, as these parameters influence phytochemical solubility, diffusion, and stability. As presented in Fig. 2, increasing the leaf-to-water ratio from 1:5 to 1:20 (g/mL) of water enhanced antioxidant activity from 48.3% to 82.6%. This improvement was associated with the greater availability of phenolics, flavonoids, tannins, and related phytochemicals capable of transferring electrons or hydrogen atoms to reactive radicals. The extract obtained using 1:20 (g/mL) represented the highest effective leaf-to-water ratio. Temperature also strongly affected phytochemical recovery. Moderate heating between 40 and 60°C promoted solvent penetration into leaf tissue and accelerated dissolution and diffusion of antioxidant constituents. Maximum activity of approximately 86.2% was obtained at 60°C. However, further heating to 80°C reduced antioxidant activity to approximately 76.9%, probably because thermally sensitive phenolic compounds and other bioactive constituents underwent oxidation or decomposition. Therefore, a 1:20 (g/mL) leaf-to-water ratio and an extraction temperature of 60°C were selected as favorable conditions for preparing the extract used in MnO_2 nanoparticle synthesis.

The temperature-dependent results indicated that prolonged exposure to elevated heat reduced the stability of bioactive compounds. Extraction time was therefore examined from 20 to 100 min using 1:20 (g/mL) leaf-to-water ratio. As illustrated in Fig. 2(c), antioxidant activity increased progressively up to 60 min because sufficient contact between the plant tissue and water promoted the diffusion of soluble phytochemicals. Extending extraction beyond 60 min decreased the measured activity, possibly because prolonged heating encouraged oxidation, structural deterioration, or volatilisation of sensitive constituents. Conversely, shorter extraction periods provided insufficient time for the solvent to penetrate the leaf tissue and release the available antioxidant compounds. The optimum combination of 1:20 (g/mL), 60 °C, and 60 min produced a maximum antioxidant activity of 86%. In a previous study, green-synthesized ZnO nanoparticles using Passiflora foetida leaf extract exhibited an antioxidant activity with an IC_{50} of 111.92 µg mL^{-1} (Loganathan *et al.* 2025). These conditions achieved effective phytochemical recovery while limiting the thermal degradation of phenolics, flavonoids, and other reducing constituents. Controlling the leaf quantity, extraction temperature, and contact duration was therefore essential for obtaining a stable, phytochemical-rich extract capable of facilitating the conversion of potassium permanganate into MnO_2 nanoparticles and supporting nanoparticle surface stabilization.

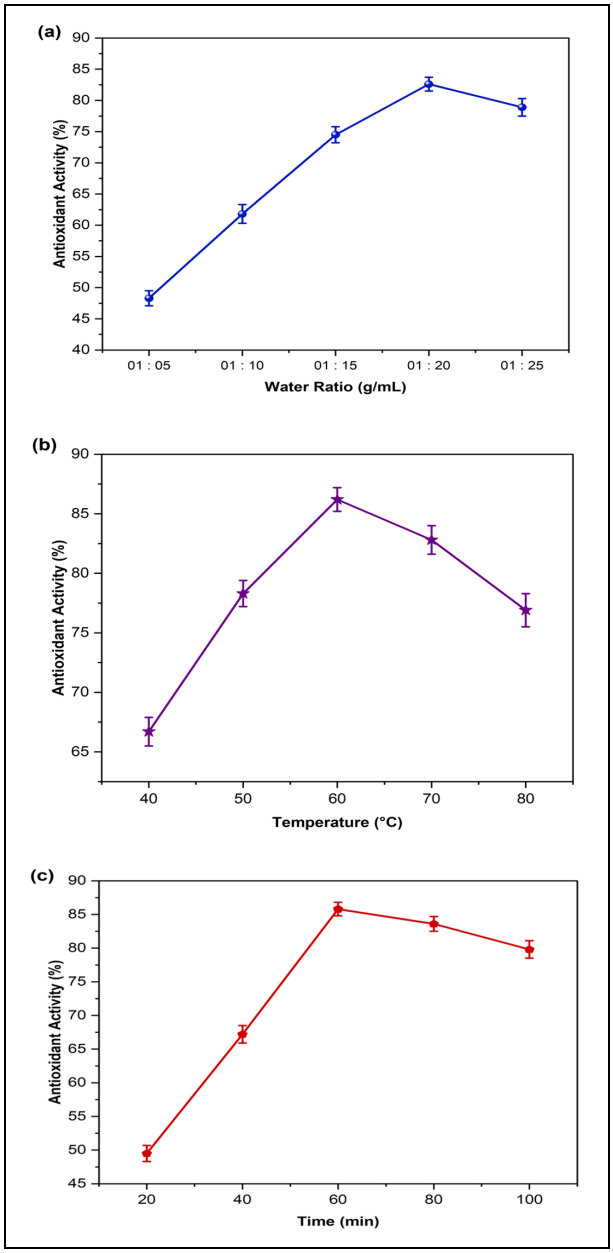

Fig. 2: Influence of (a) leaf-to-water proportion, (b) extraction temperature, and (c) extraction period on antioxidant activity of *Passiflora foetida* extract

3.1.2 UV–Visible Spectroscopic Analysis

UV–visible spectroscopy was employed as a rapid technique to monitor the conversion of potassium permanganate into MnO_2 nanoparticles in the presence of *Passiflora foetida* leaf extract. Spectra were recorded from 200 to 800 nm by a 220 UV–Vis spectrophotometer. Potassium permanganate solution initially showed a strong absorption band at approximately 525 nm, corresponding to permanganate ions. The plant extract displayed an absorption feature around 370–380 nm, which was associated with phenolic, flavonoid, and other phytochemical constituents. Following the addition of the leaf extract, the intensity of the 525 nm permanganate band gradually decreased, while a broad absorption band developed near 360–380 nm. Simultaneously, the reaction mixture changed from purple to dark brownish-black, supporting the formation of MnO_2 NPs. Spectra collected at intervals from 10 min to 24 h showed progressive attenuation of the precursor band and stabilisation of the MnO_2-related absorption feature. No appreciable spectral displacement was observed during the later reaction period (6–24 h), indicating that the reaction had reached optical stability without substantial particle aggregation. These spectral and visual changes collectively supported the successful plant-mediated formation and stabilisation of MnO_2 nanoparticles. These spectral observations are consistent with previous reports on plant-mediated MnO_2 nanoparticle synthesis. Kalopanax pictus leaf extract-mediated reduction of $KMnO_4$ similarly showed disappearance of the permanganate-specific peak with emergence of a MnO_2-specific absorption band, accompanied by a color change to dark brown, confirming the reliability of the present spectral trend (Moon *et al.* 2015).

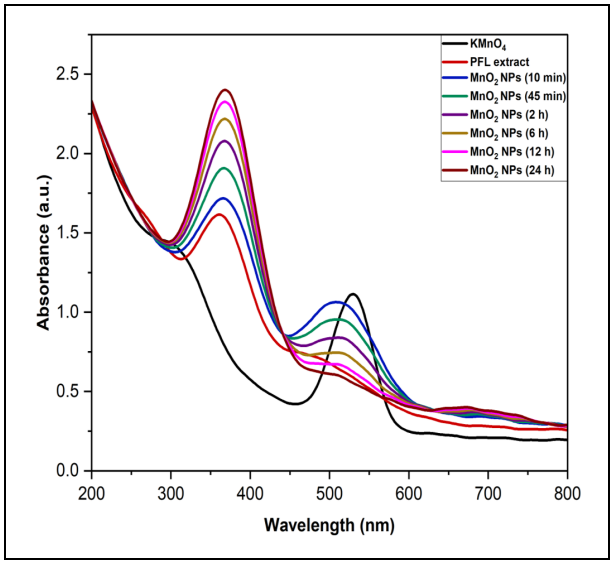

Fig. 3: Time-resolved UV–visible absorption profiles during biosynthesis of MnO_2 NPs by *Passiflora foetida* leaf extract

The optical stability of the MnO_2 suspension may be attributed to phenolic compounds, flavonoids, and other phytochemicals adsorbed at the nanoparticle surface. These constituents participate in the conversion of Mn(VII) from potassium permanganate into Mn(IV) oxide and subsequently restrict excessive particle aggregation. The gradual disappearance of the precursor band near 525 nm, together with the development of a broad absorption feature at approximately 360–380 nm, supported MnO_2 formation. Unlike metallic nanoparticles, this MnO_2 absorption should not be described as a surface-plasmon-resonance peak. It is more appropriately associated with electronic transitions involving manganese and oxygen within the oxide structure.

The reduction in the 525 nm permanganate absorption and appearance of the 360–380 nm band indicated the conversion of potassium permanganate into MnO_2. The accompanying colour transition from purple to brownish-black further supported nanoparticle formation. The broad 360–380 nm feature was consistent with nanoscale manganese oxide. However, particle dimensions and morphology cannot be determined accurately from UV–visible spectra alone and should be verified using XRD and FESEM analyses. The absence of a substantial wavelength shift during the later reaction period suggested limited aggregation and satisfactory optical stability. The coordinated spectral and colour changes demonstrated that *Passiflora foetida* extract effectively facilitated MnO_2 nanoparticle formation through an environmentally favourable aqueous process.

3.1.3 XRD Examination

The crystalline structure of MnO_2 nanoparticles was examined from 20° to 80° using a Rigaku MiniFlex 600 X-ray diffractometer, as presented in Fig. 4

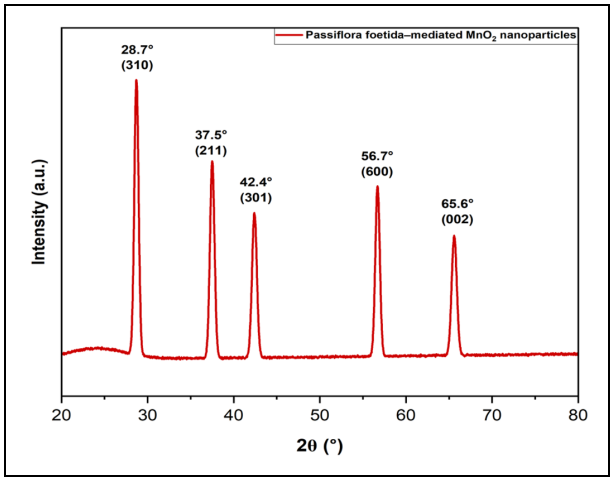

Fig. 4: X-ray diffraction pattern and crystallographic features of plant-mediated MnO_2 NPs

XRD profile of the MnO_2 nanoparticles displayed diffraction maxima at approximately 2θ = 28.7°, 37.5°, 42.4°, 56.7°, and 65.6°. These reflections were indexed to the (310), (211), (301), (600), and (002) crystallographic planes, respectively. The observed pattern supported the formation of nanocrystalline MnO_2 through the reaction between potassium permanganate and *Passiflora foetida* leaf extract. Broadened diffraction peaks indicated small crystallite dimensions and partial structural disorder, which are commonly observed in plant-mediated manganese oxide materials. Because several MnO_2 polymorphs exhibit overlapping reflections, the pattern was assigned generally to crystalline MnO_2 without claiming a single specific phase. No prominent reflections attributable to unreacted potassium permanganate or other crystalline residues were detected within the measured range. The average crystallite size was estimated from the intense reflection at 37.5° using the Debye–Scherrer relationship. The calculated value was approximately 19 nm, confirming the nanoscale crystalline structure of the prepared MnO_2 material. Overall, the observed XRD reflections confirmed the formation of nanocrystalline MnO_2; however, the specific MnO_2 polymorph could not be conclusively assigned because of overlapping diffraction peaks. The close match confirms formation of the α-MnO_2 phase via plant-mediated reduction of potassium permanganate, with minor peak shifts (<0.5°) attributable to differences in synthesis route and plant biomolecules influencing crystallite growth (Thilaga *et al.* 2025).

3.1.4 FTIR Spectral Examination

Fig. 5(a–b) presents the FTIR spectra recorded by a Thermo Scientific Nicolet iS5 spectrometer, identifying the functional groups involved in forming and stabilising MnO_2 nanoparticles with *Passiflora foetida* leaf extract.

The FTIR spectra obtained using a Thermo Scientific Nicolet iS5 spectrometer revealed several phytochemical functional groups that may participate in the formation and surface stabilisation of MnO_2 nanoparticles. In the spectrum of *Passiflora foetida* leaf extract shown in Fig. 5(a), a broad absorption band at 3385 cm^{-1} was assigned to overlapping O–H stretching vibrations from phenolic compounds, alcohols, amino acids, and proteins. The features at 2922 and 2852 cm^{-1} were assigned to symmetric and asymmetric C–H stretching, respectively. The absorption band at 1715 cm^{-1} was identified as C=O stretching, while the band at 1605 cm^{-1} was linked to the aromatic C=C stretching. The bands at 1450 and 1362 cm^{-1} were attributed to the C–H bending and O–H bending/C–O stretching, respectively. The band at 1245 cm^{-1} was attributed to C–O stretching, whereas the bands at 1173 and 1055 cm^{-1} were assigned to C–O stretching and C–O–C stretching, respectively. The band at 825 cm^{-1} was attributed to the bending of C–H out of the plane in aromatic compounds. The presence of oxygen-containing phytochemical components involved in the formation of nanoparticles and stabilisation of surfaces was suggested by these functional groups. These FTIR assignments align with previous reports on plant-mediated MnO_2 synthesis. Comparable O–H stretching (3420 cm^{-1}), phenolic C–O/O–H bending (1301 cm^{-1}), and Mn–O stretching (582 cm^{-1}) confirming α-MnO_2 formation were reported for Fe_3O_4/α-MnO_2 nanocomposites using *Pentas schimperiana* leaf extract (Kassa *et al.* 2026).

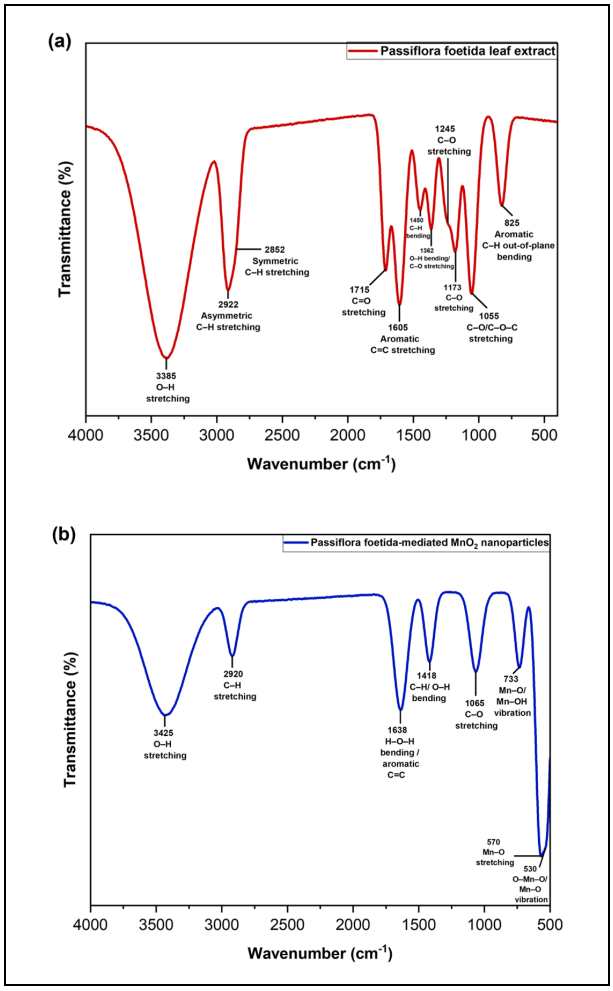

Fig. 5: FTIR spectra of (a) *Passiflora foetida* leaf extract and (b) MnO_2 nanoparticles prepared using the leaf extract

For the biosynthesised MnO_2 nanoparticles presented in Fig. 5(b), a broad band remained at 3425 cm^{-1}, which was assigned to O–H stretching. The bands observed near 2920, 1638, 1418, and 1055 cm^{-1} were associated with residual plant-derived organic molecules attached to the MnO_2 surface. Their shifts and reduced intensities relative to the leaf extract suggested the involvement of hydroxyl, carbonyl, and ether-containing groups during nanoparticle formation. More importantly, distinct low-wavenumber bands at approximately 570 and 530 cm^{-1} were assigned to Mn–O stretching and O–Mn–O/Mn–O vibration. These metal–oxygen features

supported the formation of manganese oxide. Collectively, the spectral changes indicated that phytochemicals from *Passiflora foetida* contributed to MnO_2 formation, surface functionalisation, and reduced particle aggregation. FTIR evidence should be interpreted together with XRD and EDAX results for definitive structural and elemental confirmation.

3.1.5 EDAX Analysis

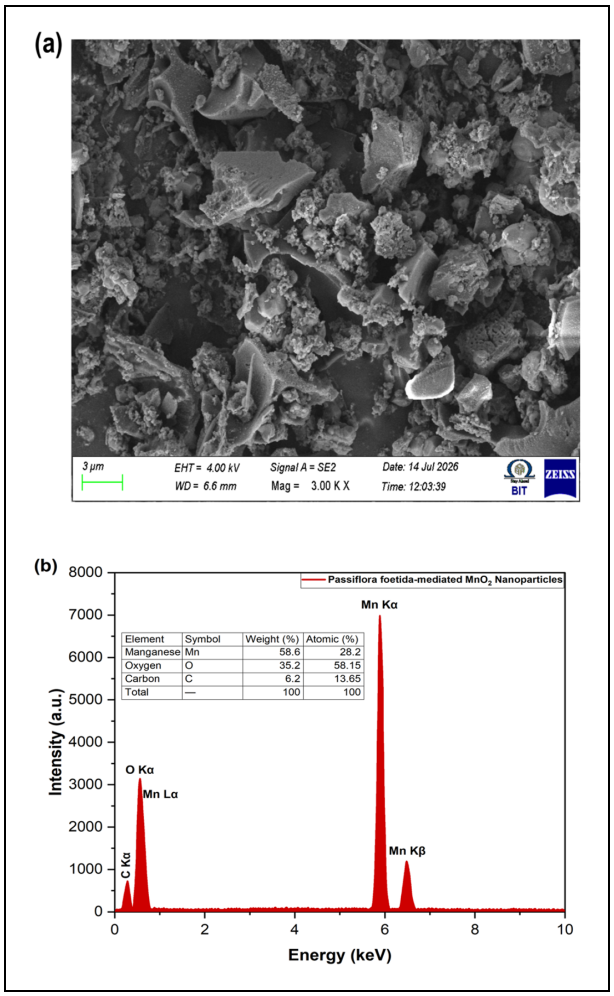

Fig. 6: (a) FESEM morphology and (b) EDAX elemental spectrum of plant-mediated MnO_2 nanoparticles

The morphology and elemental composition of the prepared MnO_2 nanoparticles were examined using a Zeiss Gemini field-emission scanning electron microscope coupled with an EDS detector. The FESEM micrograph in Fig. 6(a) displayed irregular, flake-like, and granular structures assembled into heterogeneous agglomerated clusters. This aggregation was attributed to high surface energy of nanoparticles and interactions among residual phytochemicals originating from *Passiflora foetida* leaf extract. The approximately 19 nm crystallite size obtained from XRD was smaller than the structures visible by FESEM because each observed cluster may contain several coherently diffracting crystallites.

The EDAX spectrum in Fig. 6(b) exhibited prominent manganese and oxygen signals, supporting the formation of MnO_2. A comparatively weak carbon signal was associated with plant-derived surface compounds and the conductive carbon tape employed for specimen mounting. Residual phytochemicals, including phenolic compounds, flavonoids, amino acids, and carbohydrates, may form a surface layer that restricts severe agglomeration and assists nanoparticle dispersion. EDAX confirms elemental composition but does not independently establish the oxidation state of manganese; therefore, its findings were interpreted together with XRD and FTIR results.

The nanoscale dimensions and surface characteristics of MnO_2 influenced its functional behaviour. The small crystallite size provided a relatively large surface area and more accessible sites for Rhodamine B adsorption and degradation. The broad optical absorption near 360–380 nm supported photon absorption and the generation of surface-reactive species under UV exposure. Shorter charge-transfer distances within the nanostructure may limit carrier recombination and contribute to the maximum Rhodamine B degradation efficiency of 96.34%.

The available surface sites promoted interaction between the nanoparticles and DPPH• or $ABTS^{•+}$ radicals. Surface-bound phytochemicals supplied additional electron- or hydrogen-donating groups that may strengthen radical-scavenging activity. The combined contributions of MnO_2 surface redox behaviour and plant-derived molecules were consistent with EC_{50} values of 19.84 ± 0.96 µg/mL for DPPH and 23.17 ± 1.12 µg/mL for ABTS.

3.2 Photocatalytic Performance

Operational conditions strongly affect photocatalytic efficiency because they regulate dye adsorption, light penetration, reactive-species formation, and oxidation kinetics.

3.2.1 Effect of Initial Concentration

The effect of initial Rhodamine B concentration was evaluated from 1.5×10^{-5} to 5.5×10^{-5} mol/L using MnO_2 nanoparticles at UV irradiation for 1 hour. Degradation efficiency of 99.5%, 98.8%, 97.8%, 96.5%, and 94.6% were obtained at 1.5×10^{-5}, 2.5×10^{-5}, 3.5×10^{-5}, 4.5×10^{-5}, and 5.5×10^{-5} mol/L, respectively. The optimum concentration was 3.5×10^{-5} mol/L. Further increases reduced degradation because concentrated dye molecules restricted UV penetration and competed for available MnO_2 surface sites.

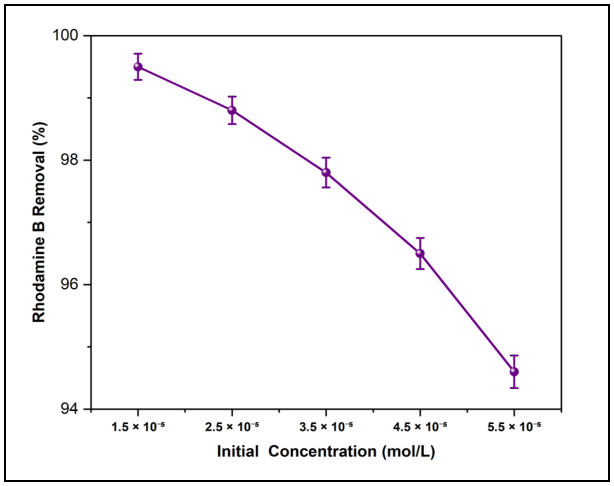

Fig. 7: Effects of initial Rhodamine B concentration

Fig. 7 shows that Rhodamine B degradation decreased up to the increasing initial dye concentration, where 97.8% removal was obtained at the lowest tested concentration of 3.5×10^{-5} mol/L, followed by a gradual decline at higher concentrations. This behaviour was governed by the following interconnected factors:

Concentrated Rhodamine B solutions absorbed and scattered more UV radiation, limiting the quantity of light reaching the MnO_2 nanoparticle surface. Consequently, fewer photocatalytically active species were generated. Excess dye molecules intercepted a larger proportion of the incident photons, thereby decreasing the radiation available for activating MnO_2 and initiating oxidation reactions. At elevated concentrations, Rhodamine B molecules increasingly covered the available MnO_2 surface sites. This restricted interactions among the dye, photocatalyst, and reactive species. The number of dye molecules increased more rapidly than the available hydroxyl and superoxide radicals. Therefore, fewer oxidative species were available for each molecule, lowering the percentage degradation. Dye molecules positioned near the illuminated region prevented radiation from reaching molecules and nanoparticles located deeper within the solution.

Therefore, although increasing the initial concentration supplied more Rhodamine B molecules for treatment, higher concentrations reduced photocatalytic efficiency through light attenuation, surface-site saturation, and competition for reactive oxidative species. The optimum among the tested initial concentrations was 3.5×10^{-5} mol/L, at which the maximum Rhodamine B removal of approximately 97.8% was achieved.

3.2.2 Influence of Solution pH

Solution pH strongly affected Rhodamine B degradation because it modified the surface chemistry of MnO_2 nanoparticles, the molecular form of dye, and production of reactive oxidative species. pH was adjusted by 0.1 M sodium hydroxide or 0.1 M hydrochloric acid. Other experimental conditions were maintained at a Rhodamine B concentration of 3.5×10^{-5} mol/L, a temperature of 30°C, and an irradiation period of 1 hour.

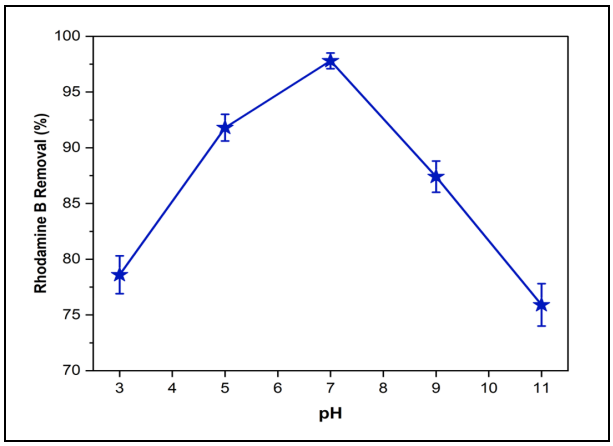

Fig. 8: Effects of solution pH

As shown in Fig. 8, degradation efficiencies of approximately 78.5%, 91.8%, 97.8%, 87.4%, and 75.8% were obtained at pH 3, 5, 7, 9, and 11, respectively. So, the optimum value was chosen as pH 7, where the maximum removal of Rhodamine B (97.8%) was obtained. The higher degradation efficiency in the near-neutral range (pH 3 to 7) suggested that the interaction occurred between Rhodamine B and the surface of MnO_2 and the produced reactive species, which facilitated the degradation of the dye structure.

Rhodamine B is predominantly a cationic dye; therefore, its behaviour should not be explained as attraction between positively charged nanoparticles and negatively charged dye molecules. Instead, the observed pH dependence resulted from the combined effects of MnO_2 surface charge, dye speciation, adsorption, and oxidation kinetics.

At alkaline pH, the MnO_2 surface became increasingly deprotonated. Although this condition can influence adsorption of cationic Rhodamine B, the lower oxidative activity and changes in reactive-species generation reduced overall degradation. Strongly alkaline conditions also promoted competition from hydroxide ions and altered the distribution of active surface sites. Consequently, Rhodamine B removal decreased from approximately 97.8% at pH 7 to 87.4% at pH 9 and 75.8% at pH 11.

3.2.3 Effect of MnO_2 Nanoparticle Dosage

The amount of MnO_2 nanoparticles employed in the reaction significantly influenced the UV-assisted degradation of Rhodamine B. To determine the optimum

catalyst loading, five dosages ranging from 10 to 50 mg were examined while maintaining the solution pH at 7.0, the initial Rhodamine B concentration at 3.5×10^{-5} mol/L, the temperature, and the irradiation period at 60 min.

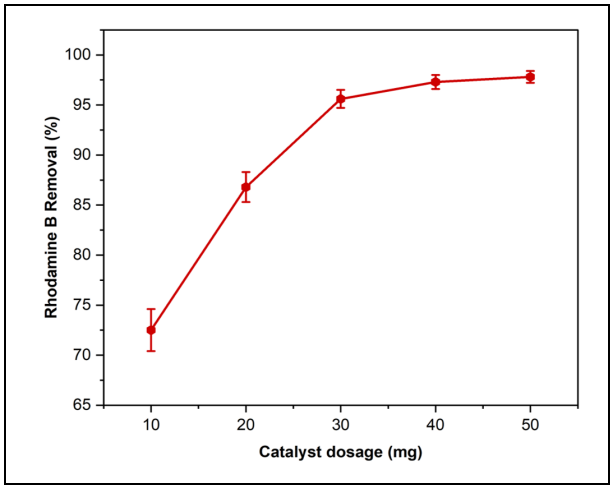

Fig. 9: Effects of MnO_2 nanoparticle dosage

As illustrated in Fig. 9, degradation efficiencies of 72.5%, 86.7%, 95.6%, 97.3%, and 97.8% were obtained using catalyst dosages of 10, 20, 30, 40, and 50 mg, respectively. The highest degradation efficiency was therefore recorded at an optimum MnO_2 dosage of 50 mg.

Increasing the catalyst quantity from 10 to 50 mg enhanced degradation because a greater number of MnO_2 nanoparticles became available in the reaction medium. This increase supplied larger effective surface area and accessible active sites for Rhodamine B adsorption. Under UV irradiation, the additional photoactive sites promoted the production of reactive oxidative species and increased contact among the dye molecules, catalyst surface, and generated radicals. Consequently, the degradation efficiency increased progressively and reached 97.8% at 50 mg.

However, increasing the MnO_2 dosage beyond 30 mg resulted in only a marginal improvement in Rhodamine B removal. The degradation efficiency was 95.6% at 30 mg, 97.3% at 40 mg and 97.8% at 50 mg. Most of the photoactive sites were already effective at 30 mg, and subsequent additions of catalyst only resulted in a small increase in the photoactive-species generation. Thus, the maximum degradation efficiency (97.8%) was obtained at a catalyst loading of 50 mg, and further increase in the catalyst loading resulted in only marginal improvement in the photocatalytic performance.

Satisfactory dispersion preserves the accessible MnO_2 surface area and facilitates contact between Rhodamine B molecules and active catalytic sites. Severe aggregation decreases the effective number of reaction sites. An appropriate catalyst dosage allows UV radiation to penetrate the suspension and activate a large proportion of the MnO_2 nanoparticles. Excessive loading produces turbidity, scattering, and self-shading. Increasing the dosage up to 50 mg enhances the generation of surface-reactive oxidative species. Above this amount, light limitation and charge-carrier recombination restrict further improvement. Selecting 50 mg provides the highest degradation efficiency. This dosage offers a suitable balance between available surface area, light penetration, nanoparticle dispersion, and reactive-species production. Plant-derived surface compounds from *Passiflora foetida* may assist nanoparticle dispersion and reduce rapid agglomeration. This stability is important for maintaining MnO_2 activity during repeated wastewater-treatment operations.

Therefore, a higher MnO_2 loading promoted Rhodamine B degradation, whereas excessive quantities may lower performance through aggregation, increased turbidity, restricted photon penetration, and particle self-shielding.

3.2.4 Effect of Reaction Temperature

The influence of temperature on Rhodamine B degradation was investigated using 50 mg of biosynthesised MnO_2 nanoparticles in 50 mL of a 3.5×10−5 mol/L dye solution. Experiments were conducted at 15, 30, 45, 60, and 75 °C for 1 hour under UV irradiation, as shown in Fig. 10.

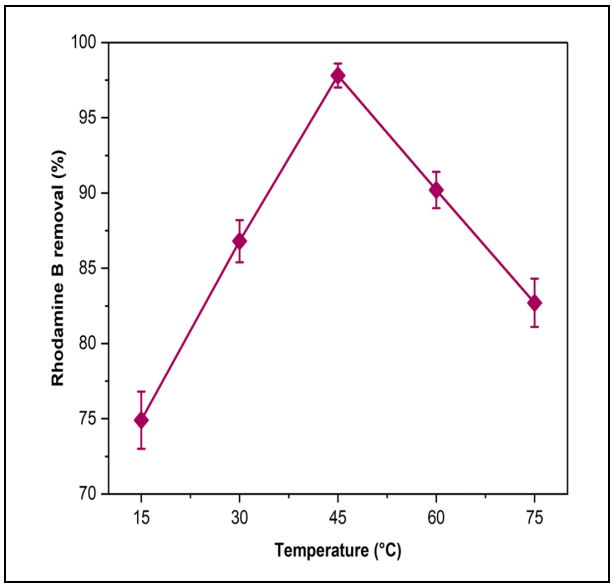

Fig. 10: Effects of reaction temperature

The corresponding degradation efficiencies were 74.8%, 86.8%, 97.8%, 90.2%, and 82.7%, respectively. These results demonstrated that photocatalytic performance initially improved with increasing temperature, reached its maximum at 45 °C, and subsequently declined at higher temperatures. The improvement observed between 15 and 45 °C was associated with increased molecular kinetic energy.

Moderate heating enhanced the diffusion of Rhodamine B molecules through the liquid phase and promoted more frequent collisions with active sites on the MnO_2 nanoparticle surface. Improved mass transfer also facilitated the adsorption of dye molecules and their interaction with surface-generated oxidative species. Consequently, increasing the reaction temperature to 45 °C accelerated the overall degradation process and produced the maximum efficiency of 97.8%.

However, temperatures above 45 °C adversely affected the photocatalytic reaction. Excessive heating can weaken adsorption of Rhodamine B molecules at MnO_2 surface, thereby reducing contact required for efficient oxidation. Higher temperatures may also decrease the solubility of dissolved oxygen, limiting oxygen-derived reactive species involved in degradation. Moreover, accelerated charge-carrier recombination and destabilisation of surface-bound reaction intermediates can reduce the availability of oxidising species. These combined effects explain the decline to 90.2% at 60 °C and 82.7% at 75 °C. The decrease at elevated temperature should not be attributed mainly to solvent evaporation, because the reaction volume must be maintained during controlled photocatalytic experiments. Similarly, the increase up to 45 °C alone does not conclusively establish that the reaction is endothermic; a thermodynamic analysis would be required for such a conclusion. The results instead demonstrate that 45 °C provides a favourable balance among molecular diffusion, dye adsorption, oxygen availability, surface-reaction kinetics, and reactive-species production. Maintaining this optimum temperature is therefore important for achieving efficient Rhodamine B degradation using MnO_2 nanoparticles.

3.2.5 Effect of Irradiation Time

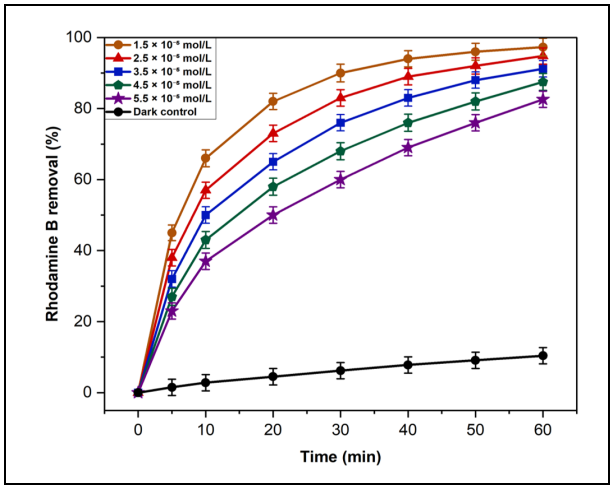

Fig. 11: Effects of irradiation time on Rhodamine B degradation

The influence of irradiation time on Rhodamine B degradation was investigated using 50 mg of biosynthesised MnO_2 nanoparticles over a reaction period of $0-60$ min, the remaining experimental conditions were maintained constant. The initial Rhodamine B concentration was 3.5×10^{-5} mol/L, the pH was maintained at 7.0, and the reaction temperature was controlled at 45°C.

As displayed in Fig. 11, degradation efficiencies of 0%, 42.3%, 65.8%, 81.7%, 90.6%, 95.4%, and 97.8% were recorded after $0, 10, 20, 30, 40, 50$ and 60 min of UV exposure.

Rhodamine B removal proceeded rapidly during the first 30 min because numerous unoccupied active sites were initially available on the MnO_2 nanoparticle surface. This condition promoted rapid dye adsorption and close interaction between Rhodamine B molecules and photogenerated oxidative species. The initially high dye concentration also increased the probability of contact between the pollutant molecules and active catalyst sites. Consequently, approximately 81.7% degradation was achieved within the first 30 min, accompanied by a progressive decrease in the characteristic pink colour of the solution.

After 30 min, the degradation rate gradually declined and approached a plateau between 50 and 60 min. This reduction did not indicate that degradation products were being generated at the same rate as Rhodamine B. Instead, the decreasing reaction rate was associated with the lower concentration of undegraded dye remaining in the solution. In addition, intermediate products formed during Rhodamine B oxidation may temporarily occupy MnO_2 surface sites and compete with the parent dye for reactive species. As fewer dye molecules remained available, collisions among Rhodamine B, active sites, and oxidizing radicals became less frequent.

At 60 min, degradation efficiencies of 99.5%, 98.8%, 97.8%, 96.5%, and 94.6% were obtained for initial Rhodamine B concentrations of 1.5×10^{-5}, 2.5×10^{-5}, 3.5×10^{-5}, 4.5×10^{-5}, and 5.5×10^{-5} mol/L, respectively. The lower efficiencies observed at elevated concentrations resulted from restricted UV penetration, increased competition for MnO_2 active sites, and insufficient reactive species relative to the number of dye molecules. These findings established 60 min as the selected irradiation period, although most degradation occurred during the initial 30-50 min.

3.3 Kinetics of Dye Photodegradation

The degradation kinetics of Rhodamine *B* were evaluated by dispersing 50 mg of biosynthesised MnO_2 nanoparticles in 50 mL of a 3.5 ×ye solution. The reaction was performed at pH 7.0 ad 45°C for 1 hour under UV irradiation. Aliquots were collected at predetermined time intervals, and residual Rhodamine B

concentration was determined from its absorbance at 554 nm. Kinetic data was fitted by apparent pseudo-first and second-order models to identify expression that most accurately represented concentration decrease during photocatalytic treatment. Similarly, green-synthesized SiO_2–MnO_2 nanocomposites prepared using Ebenopsis ebano leaf extract achieved 74.77% acetamiprid degradation within 90 min under 365 nm UV irradiation, following pseudo-first-order kinetics (k = 0.01472 min^{-1}) (Bandral *et al.* 2026)

3.3.1 Kinetic Modelling of Rhodamine B Photodegradation Using MnO_2 Nanoparticles

The pseudo-first-order model assumes that the degradation rate was directly proportional to Rhodamine B concentration remaining in the reaction medium. Its integrated linear expression is presented in Equation (3) (Deepha and Senthilnathan, 2026b):

$$\ln\left(\frac{C_0}{C_t}\right) = k_1 t \qquad \dots (3)$$

C_0 were the initial Rhodamine B concentration, C_t were the concentration after irradiation time t, and k_1 were the apparent pseudo-first-order rate constant expressed in min^{-1}. A plot of $\ln(C_0/C_t)$ against time was used to calculate k_1 from the slope.

3.3.2 Pseudo-Second-Order Model

The pseudo-second-order model assumes the degradation rate depends on the square of the residual Rhodamine B concentration. The integrated form is expressed by Equation (4) (Gaddala *et al.* 2025):

$$\frac{1}{C_t} - \frac{1}{C_0} = k_2 t \qquad \dots (4)$$

where C_0 and C_t shows time-dependent and initial dye concentrations, while k_2 were apparent pseudo-second-order rate constants in $\text{Lmol}^{-1}\ \text{min}^{-1}$. The value of k_2 was obtained from the slope of $1/C_t - 1/C_0$ plotted against irradiation time.

Both models were compared using their coefficients of determination and fitting errors. The model showing the higher R^2 and lower error was considered more suitable for describing Rhodamine B degradation. However, agreement with either kinetic expression alone does not prove that adsorption or a particular elementary reaction controls the overall photocatalytic mechanism.

Table 2. Kinetic parameters (rate constants, R^2, RMSE, SSE) for pseudo-first-order and pseudo-second-order model fits

Kinetic model	Linear Equation	Rate Constant	R^2	RMSE*	SSE*
Pseudo-first-order	$\ln(C_0/Ct)=0.06357t-0.10980$	$k_1=0.06357\ \text{min}^{-1}$	0.9958	0.0826	0.0477
Pseudo-second-order	$1/C_t=18478.57t-191281.54$	$k_2=1.8479\times104\ \text{L mol}^{-1}\ \text{min}^{-1}$	0.7489	2.1400×10^5	3.205×10^{11}

The calculated kinetic parameters for Rhodamine B degradation are presented in Table. The pseudo-second-order model exhibited a higher coefficient of determination and a lower fitting error than the pseudo-first-order model, demonstrating its better agreement with the experimental data. However, this statistical agreement represents the overall apparent degradation behaviour and does not independently confirm the elementary photocatalytic mechanism.

Kinetic analysis demonstrated that pseudo-second-order model produced linear correlation coefficients (R^2) from 0.987 to 0.994, indicating excellent agreement with the experimental Rhodamine B degradation data. The concentrations predicted by this model were also close to the measured residual dye concentrations. In comparison, pseudo-first-order model generated lower R^2 and showed greater deviations between calculated and experimental results. Therefore, pseudo-second-order expression provided accurate mathematical representation of concentration-dependent degradation behaviour.

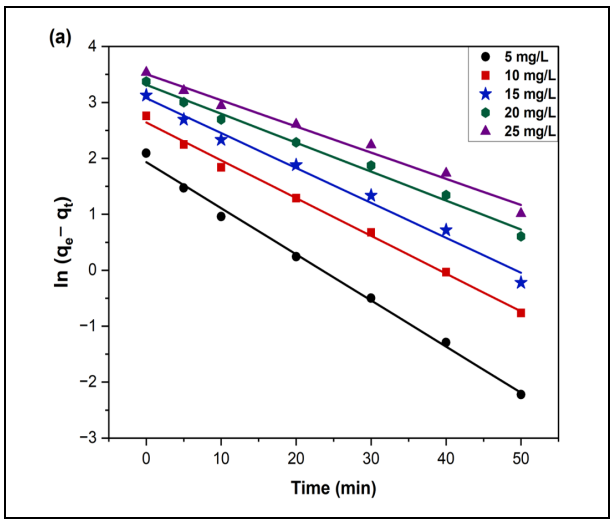

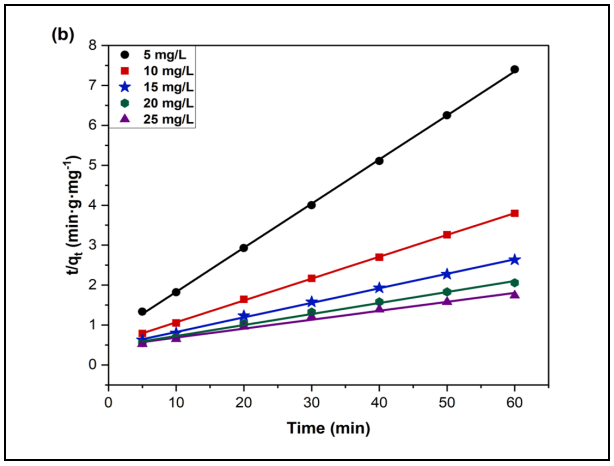

Fig. 12: Linear kinetic fitting of Rhodamine B degradation by biosynthesised MnO_2 nanoparticles: (a) pseudo-first and (b) Second-order models

Although, the superior pseudo-second-order fit indicates that the reaction rate had a nonlinear dependence on the residual Rhodamine B concentration, it does not independently confirm chemisorption as the rate-controlling mechanism. Photocatalytic degradation involves several simultaneous stages, including dye transport, surface adsorption, photon absorption, charge-carrier generation, reactive-species formation, and oxidation of the adsorbed molecules. Consequently, kinetic-model agreement alone cannot establish chemical bonding or electron exchange between the dye and MnO_2 surface.

The non-zero intercept observed in the pseudo-second-order plot may originate from rapid adsorption during the initial dark-equilibration stage, variations in photon availability, intermediate-product formation, or external mass-transfer resistance. Surface adsorption can assist photocatalysis by bringing Rhodamine B molecules closer to reactive sites; however, it should not be interpreted as the only rate-limiting step. The high R^2 values instead demonstrate that pseudo-second-order model were suitable for predicting overall apparent degradation kinetics under the investigated conditions.

3.3.3 Proposed Mechanism of Rhodamine B Photodegradation

The proposed UV-assisted oxidation pathway of Rhodamine B using plant-mediated MnO_2 nanoparticles. Their nanoscale structure and accessible surface sites promote dye adsorption and interfacial reactions. Under UV irradiation, MnO_2 absorbs photon energy and generates excited charge carriers. Photogenerated holes can react with surface water or hydroxyl groups to form hydroxyl radicals, whereas electrons interact with dissolved oxygen to form oxygen-derived reactive species. These oxidants attack the Rhodamine B chromophore, initiate de-ethylation and cleavage of the conjugated structure, and subsequently transform the dye into smaller intermediate compounds. Continued oxidation can ultimately produce carbon dioxide, water, and inorganic ions.

When MnO_2 nanoparticles are exposed to UV radiation with energy equal to or greater than their effective band-gap energy, electrons are promoted from the valence band to the conduction band, leaving positive holes behind. This photoexcitation produces electron-hole pairs capable of initiating surface reduction and oxidation reactions.

The resulting radicals are short-lived but highly reactive. They attack the conjugated xanthene structure of Rhodamine B, causing chromophore cleavage, de-ethylation, ring opening, and progressive formation of smaller organic intermediates. Continuous exposure to reactive oxidative species may further transform these intermediates into water, carbon dioxide, and inorganic ions. Process should therefore be described as photocatalytic oxidation or degradation rather than photocatalytic reduction.

Unlike systems involving redox-active dissolved metal ions, the proposed MnO_2 pathway does not require an iron-mediated Fenton cycle. Hydrogen peroxide may still be formed through reactions involving oxygen-derived radicals and can subsequently contribute to additional hydroxyl-radical generation. However, the relative contributions of holes, hydroxyl radicals, and superoxide radicals should be verified using scavenger experiments before identifying a single dominant pathway.

The proposed reaction sequence is represented by Equations (5)-(12).

Step 1: Photoexcitation.

$$MnO_2 + h\nu \rightarrow e^-_{CB} + h^+_{VB} \quad \ldots (5)$$

Step 2: Formation of superoxide

$$e^-_{CB} + O_2 \rightarrow O_2^{\cdot} \quad \ldots (6)$$

Step 3: Production of hydroxyl

$$h^+_{VB} + H_2O \rightarrow {}^{\cdot}OH + H^+ \quad \ldots (7)$$

$$h^+_{VB} + OH^- \rightarrow {}^{\cdot}OH \quad \ldots (8)$$

Step 4: Initial oxidation of Rhodamine B

$$C_{28}H_{31}ClN_2O_3 + O_2^{\cdot -} \rightarrow \text{ oxidation intermediates} \ldots (9)$$

$$C_{28}H_{31}ClN_2O_3 + {}^{\cdot}OH \rightarrow \text{oxidation intermediates} \ldots (10)$$

Step 5: Further oxidation of intermediate compounds

$$\text{Intermediates} + {}^{\cdot}OH + O_2^{\cdot} \rightarrow CO_2 + H_2O + \text{inorganic ions} \quad \ldots (11)$$

Step 6: Schematic overall degradation pathway

$$\text{Rhodamine B} + O_2 + H_2O \xrightarrow[MnO_2]{h\nu} CO_2 + H_2O + Cl^- + \text{nitrogen containing ions} \quad \ldots (12)$$

Equation (12) is a schematic representation rather than a stoichiometrically balanced mineralization equation. Complete mineralization should be claimed only when supported by total organic carbon or equivalent analysis.

3.4 Antioxidant Performance

Fig. 13(a-b) presents ABTS and DPPH radical-scavenging activity of biosynthesised MnO_2 nanoparticles.

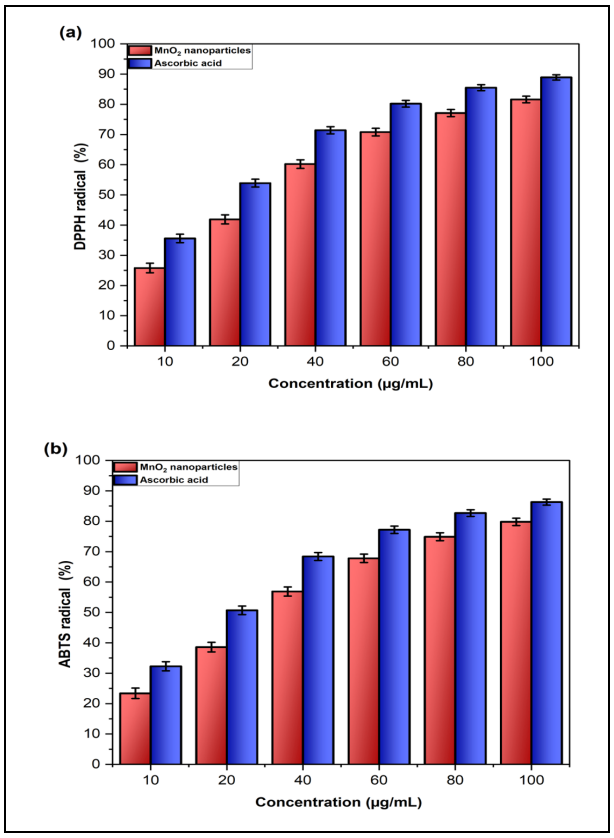

Fig. 13: Concentration-dependent antioxidant performance of biosynthesised MnO_2 nanoparticles determined by (a) DPPH and (b) ABTS radical-scavenging assays

Antioxidant activity of biosynthesised MnO_2 nanoparticles was investigated using ABTS and DPPH free-radical scavenging assays. In both tests, scavenging efficiency increased progressively with nanoparticle concentration, demonstrating dose-dependent antioxidant behaviour. This response may be associated with the increasing availability of redox-active surface sites and residual phytochemicals derived from *Passiflora foetida* leaf extract. Phenolic, hydroxyl, carbonyl, and other surface functional groups can participate in electron or hydrogen transfer and thereby contribute to radical neutralization.

The MnO_2 nanoparticles produced EC_{50} values of 31.46 ± 1.08 µg/mL in the DPPH assay and 35.18 ± 1.15 µg/mL in the ABTS assay. By comparison, ascorbic acid exhibited corresponding EC_{50} values of 24.83 ± 0.97 and 28.54 ± 1.03 µg/mL. Compared with a previous study, green-synthesized MnO_2 nanoparticles derived from Cordia myxa fruit extract showed significant antioxidant activity in DPPH and FRAP assays at 150 µg mL^{-1} (Manjhi *et al.* 2025). Because a lower EC_{50} value represents stronger radical-scavenging activity, ascorbic acid remained more effective than the nanoparticle samples. Nevertheless, the relatively close values confirmed that the prepared MnO_2 nanoparticles possessed considerable antioxidant potential. The difference between the DPPH and ABTS results may arise from variations in radical structure, solvent environment, surface accessibility, and the reaction kinetics of the antioxidant constituents. Nanoparticle dimensions, surface oxidation states, phytochemical coverage, and aggregation can also influence the number of accessible reactive sites. Therefore, the measured activity was probably produced by the combined redox behaviour of MnO_2 and the plant-derived compounds attached to its surface. These results do not independently demonstrate biocompatibility or suitability for food and biomedical applications. Cytotoxicity, nanoparticle migration, long-term stability, and safety assessments would be required before incorporating MnO_2 nanoparticles into gelatin-based packaging or biological materials. Sample blanks should also be included to correct for nanoparticle absorption and light scattering during spectrophotometric measurements.

3.5 Reusability of Biosynthesised MnO_2 Nanoparticles

The recyclability of the biosynthesised MnO_2 nanoparticles was evaluated during UV-assisted Rhodamine B degradation. Each experiment employed 50 mg of catalyst in 50 mL of 3.5×10^{-5} mol/L Rhodamine B at pH 7.0 and 45 °C for 60 min. After every degradation cycle, the MnO_2 nanoparticles was separated from reaction mixture by centrifugation. The recovered material was repeatedly washed by double-distilled water and ethanol to eliminate adsorbed dye molecules and oxidation intermediates, followed by drying before reuse.

The regenerated MnO_2 catalyst was examined over five consecutive degradation cycles under identical experimental conditions. This procedure enabled evaluation of activity retention, structural stability, catalyst loss, surface fouling, and possible blockage of reactive sites. A gradual decline during repeated use may

result from incomplete recovery, residual intermediates, nanoparticle aggregation, or changes in surface-active groups.

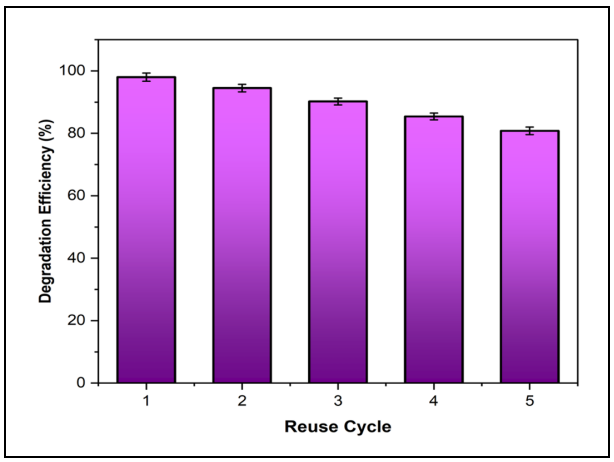

Fig. 14: Photocatalytic stability of biosynthesised MnO_2 nanoparticles over five consecutive Rhodamine B degradation cycles

Small aliquots were withdrawn from the reaction mixture at predetermined intervals, and their absorbance was measured at 554 nm to monitor residual Rhodamine B. From fig. 14, degradation efficiencies of 97.5%, 94.3%, 89.8%, 85.2%, and 80.5% were obtained during the first, second, third, fourth, and fifth cycles, respectively. Only a minor reduction occurred during the first three cycles, indicating that the MnO_2 nanoparticles retained substantial photocatalytic activity during repeated treatment. A more noticeable decline was observed after the third cycle. This reduction may have resulted from incomplete catalyst recovery, nanoparticle aggregation, and accumulation of Rhodamine B degradation intermediates on the MnO_2 surface. These residual compounds can block active sites, reduce light absorption by the catalyst, and restrict interactions with reactive oxidative species. Repeated washing and centrifugation may also cause a small loss of catalyst mass during each recovery stage. Nevertheless, the MnO_2 nanoparticles maintained 80.5% degradation efficiency after the fifth cycle, demonstrating satisfactory short-term recyclability. Additional XRD, FTIR, or surface analysis of the recovered material would be required to confirm structural stability after repeated use.

3.6 Mechanical Behaviour of Gelatin–MnO_2 Films

The stress–strain responses of the pure gelatin film (S1) and MnO_2-reinforced films (S2–S5) demonstrated that nanoparticle loading influenced elongation at break, elastic modulus, and tensile strength. At the lower MnO_2 quantities of 1000–2000 µg used in S2 and S3, elastic modulus and tensile strength lowered relative to S1. This behaviour was attributed to incomplete nanoparticle dispersion and weak interfacial interactions between the gelatin chains and MnO_2 surface. At low loading, isolated nanoparticle clusters may act as local stress-concentration points instead of uniformly transferring the applied load through the gelatin matrix. These discontinuities interrupt polymer-chain interactions and reduce film cohesion, leading to premature deformation or failure. A reduction in elastic modulus indicates lower stiffness, whereas a decrease in elongation at break indicates reduced ductility; these properties should not be interpreted as equivalent. At the higher loadings used in S4 and S5, more extensive interactions between MnO_2 surface groups and gelatin functional groups may improve stress transfer, provided that severe agglomeration is avoided. Fig. 15 compares the complete stress–strain behaviour of all five film formulations.

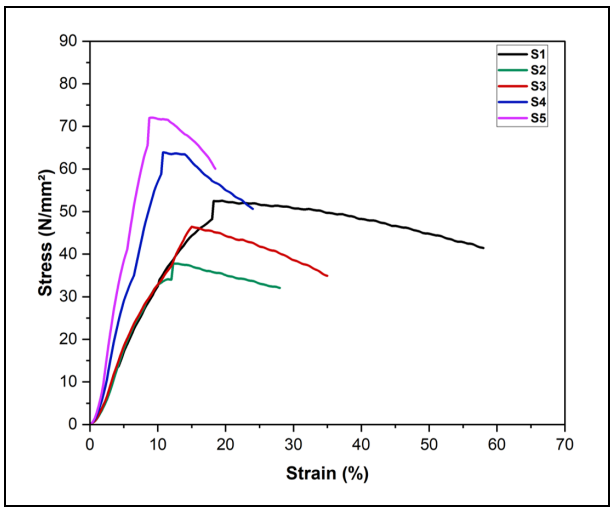

Fig. 15: Stress–strain curves of pure gelatin and MnO_2-reinforced gelatin films (S1–S5)

Fig. 16 compares the tensile strength of the prepared gelatin–MnO_2 nanocomposite films.

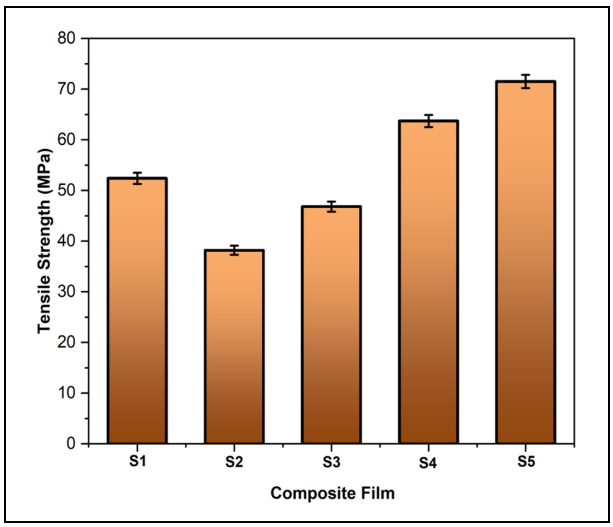

Fig. 16: Tensile strength of pure gelatin and MnO_2-reinforced gelatin films (S1–S5)

Table 3. Tensile strength, elastic modulus, and elongation at break of samples with varying MnO_2 content

Sample	MnO_2 (µg)	Tensile Strength (MPa)	Elastic Modulus (MPa)	Elongation at Break (%)
S1	0	52.3 ± 1.1	310 ± 16	58.0 ± 1.4
S2	1000	38.1 ± 0.8	430 ± 16	28.0 ± 1.1
S3	2000	46.7 ± 1.0	520 ± 19	35.0 ± 1.3
S4	3000	63.5 ± 1.2	690 ± 23	24.0 ± 0.9
S5	4000	71.5 ± 1.4	845 ± 27	18.5 ± 0.9

Increasing the MnO_2 nanoparticle quantity to 3000–4000 µg markedly altered the mechanical performance of the gelatin films. The higher tensile strength of S4 and S5 indicated more effective reinforcement of the polymer network. At these loadings, hydroxyl-containing groups on the MnO_2 surface may establish stronger hydrogen-bonding and secondary interactions with amino, hydroxyl, and carbonyl groups in gelatin. These interfacial interactions produce a denser structure and enable the nanoparticles to transfer applied stress throughout the film matrix. Consequently, the reinforced films withstand greater tensile forces before failure. However, the elastic modulus remained comparatively stable despite the improvement in strength, suggesting that additional MnO_2 enhanced load-bearing capacity without substantially changing film stiffness. This behaviour may occur when the gelatin network approaches its effective reinforcement limit. Compared with the pure gelatin film, elongation at break decreased across all MnO_2-containing formulations (1000–4000 µg), indicating restricted polymer-chain mobility and reduced ductility, as presented in Fig. 17.

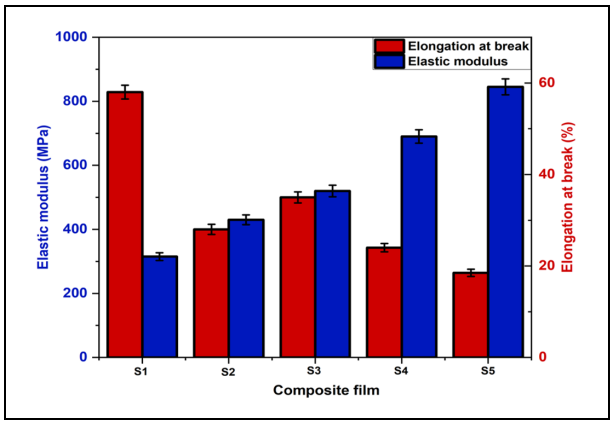

Fig. 17: Variation in elongation at break and elastic modulus of gelatin films containing different MnO_2 nanoparticle loadings (S1–S5)

The reduced flexibility indicated that MnO_2 incorporation restricted molecular movement within the gelatin network, limiting polymer-chain rearrangement under tensile loading. The nanoparticles functioned as physical junction points through interfacial interactions with gelatin functional groups, producing a more constrained film structure. Consequently, the nanocomposite films became less extensible and failed at lower strain levels. This behaviour is commonly observed when rigid nanofillers reinforce polymer matrices: tensile strength may improve, whereas elongation at break decreases because chain mobility is suppressed. Therefore, MnO_2 addition produced a clear balance between mechanical strength and film flexibility, enhancing load-bearing performance while reducing ductility at higher nanoparticle quantities.

4. CONCLUSIONS

This study demonstrated the successful plant-assisted synthesis of nanoparticles using *Passiflora foetida* leaf extract, yielding a crystalline material with an average crystallite size of approximately 19 nm and irregular flake-like and granular structures. The elemental composition and surface functional groups supported the successful formation and stabilization of the nanoparticles. The synthesized nanoparticles exhibited excellent photocatalytic activity toward Rhodamine B, achieving a maximum degradation efficiency of 97.8% at pH 7.0 and retaining 80.5% efficiency after five consecutive cycles, indicating satisfactory reusability. Significant antioxidant activity was also observed, with IC_{50} values of 31.46 ± 1.08 and 35.18 ± 1.15 µg/mL for the DPPH and ABTS assays, respectively. Among the gelatin-based formulations, S5 demonstrated the highest tensile strength of 71 MPa and elastic modulus of 845 MPa, highlighting the reinforcing potential of the nanoparticles in biodegradable films. Overall, the developed *P. foetida*-mediated nanoparticles showed promising multifunctional properties for photocatalytic treatment and sustainable packaging applications. Future investigations should focus on nanoparticle toxicity, manganese leaching, degradation by-products, long-term stability, performance in real wastewater, extended recyclability, film safety and biodegradability, and process scalability to establish their environmental safety and practical applicability.

FUNDING

This research received no specific grant from any funding agency in the public, commercial, or not-for-profit sectors.

CONFLICTS OF INTEREST

The authors declare that there is no conflict of interest.

COPYRIGHT

This article is an open-access article distributed under the terms and conditions of the Creative Commons Attribution (CC BY) license (http://creativecommons.org/licenses/by/4.0/).

CC BY

REFERENCES

Bandral, S., Bharti, R., Koul, U. and Sharma, R. Green synthesis of SiO_2-MnO_2 nanocomposite from Ebenopsis ebano leaves and its application in the photocatalytic degradation of acetamiprid, *J. Photochem. Photobio. A: Chem.*, 481, 117440 (2026). https://doi.org/10.1016/j.jphotochem.2026.117440

Blessymol, B., Kalaiselvi, V., Yasotha, P. and Gopi, S., Comparative Study of Chemically and Green Synthesized Titanium Dioxide Nanoparticles using *Leucas aspera* Leaf Extract, *J. Environ. Nanotechnol*., 12(3), 10-13 (2023). https://doi.org/10.13074/jent.2023.09.233471

Chiam, S. L., Leo, C. P., Pung, S. Y. and Ang, W. L., Modulation of MnO_2-BiOCl photocatalyst immobilized in polyvinyl alcohol hydrogel for reusable photodegradation of Rhodamine B and Ibuprofen under visible light, *Solid State Sci.,* 160, 107831 (2025). https://doi.org/10.1016/j.solidstatesciences.2025.107831

Deepha, R. and Senthilnathan, V., Photocatalytic Degradation Analysis of Rhodamine B and Eosin Yellow Dyes using Ag-doped TiO_2 Nanoparticles Synthesized via Sol-gel Method, *J. Environ. Nanotechnol.,* 15(1), 682–691 (2026b). https://doi.org/10.13074/jent.2026.03.2612097

Gaddala, B., Devi, K. V, Balakrishnan, V., Sundramurthy, V. P., Hariprabhu, M., Mayakannan, S., Kadaikunnan, S. and Khaled, J. M., Evaluation of detoxification performance of Pithecellobium dulce seed pod powder upon acid treatment: removal of reactive red 195-A dye and kinetic analysis, *Zeitschrift Fur Physikalische Chemie*, 239(6), 885–910 (2025). https://doi.org/10.1515/zpch-2024-0879

Gao, Y., He, W., Wang, H., Shan, C., Du, Y., Gao, X., Han, L. and Zhang, R., MnO_2-Mediated Fluorescence Recovery for Selective Detection of Glutathione Using Orange-Emitting Carbon Quantum Dots, *J. Fluores.*, 36(1), 679–688 (2026). https://doi.org/10.1007/s10895-025-04604-4

Hakimi, M., Hosseini, H. A. and Elhaminezhad, B., Fabrication of Manganese Dioxide Nanoparticles in Starch and Gelatin Beds: Investigation of Photocatalytic Activity, *Chem. Methodol.*, 8(1), 37–46 (2024). https://doi.org/10.48309/chemm.2024.424921.1739

Jeoffrey, A. C., Ramalingam, S. J., Murugaiah, K. and Balu, A. R., Highly photoactive rGO-MnO_2/CuO nanocomposite photocatalyst for the removal of metanil yellow dye and bacterial resistance against *Pseudomonas Aeruginosa*, *Chem. Phy. Impact*, 6, 100246 (2023). https://doi.org/10.1016/j.chphi.2023.100246

Kassa, M. E., Zereffa, E. A., Gindose, T. G. and Zeleke, T. D., Eco-friendly fabrication of Fe_3O_4/α-MnO_2 nanocomposites using Pentas schimperiana leaf extract for enhanced biomedicinal and environmental applications, *Sci. Rep.*, 16(1), 5078 (2026). https://doi.org/10.1038/s41598-025-34955-8

Khan, M., Ware, P. and Shimpi, N., Synthesis of ZnO nanoparticles using peels of *Passiflora foetida* and study of its activity as an efficient catalyst for the degradation of hazardous organic dye, *SN Appl. Sci.*, 3(5), 528 (2021). https://doi.org/10.1007/s42452-021-04436-4

Loganathan, A., Sethupathi, N., Mahalingam, P. and Sivakumar, P., Green Synthesis, Structural Characterization and Kinetics of Photocatalytic Degradation of Reactive Blue 19 Dye Using CeO_2-doped Reduced Graphene Oxide Nanohybrid, *J. Environ. Nanotechnol.*, 15(1), 576–585 (2026). https://doi.org/10.13074/jent.2026.03.2612126

Loganathan, S., Selvam, K., Govindasamy, M. and Habila, M. A., Bioynthesis and characterization of zinc oxide nanoparticles (ZnO-NPs) using *Passiflora foetida* Linn leaves extract and their biological applications, *Biomass Convers. Biorefine*, 15(4), 5861–5871 (2025). https://doi.org/10.1007/s13399-024-05593-3

Manjhi, M. K., Kumar, H., Pathak, A., Gauliya, K., Mandal, N., Upadhyay, D. C., Yadav, V., Saad, T. and Upadhyay, C. P., Green Fabrication of Manganese Oxide Nanoparticles and its Application in Mitigating Antimicrobial Resistance, *J. Clust. Sci.*, 36(6), 218 (2025). https://doi.org/10.1007/s10876-025-02927-7

Mei, Y., Huang, Y., Xu, H., Yang, W. and Lin, X., Thin film composite membrane with self-cleaning properties via a catalytic interlayer for dye wastewater treatment, *J. Membra. Sci.*, 688, 122107 (2023). https://doi.org/10.1016/j.memsci.2023.122107

Moon, S. A., Salunke, B. K., Alkotaini, B., Sathiyamoorthi, E. and Kim, B. S., Biological synthesis of manganese dioxide nanoparticles by Kalopanax pictus plant extract, *IET Nanobiotechnol.*, 9(4), 220–225 (2015). https://doi.org/10.1049/iet-nbt.2014.0051

Mungle, N. P., Deshmukh, M. S., Satishkumar, P., Talodhikar, V., Kakade, N. T., Clement, M. and Gounder, K. N., Green Synthesis of $MnFe_2O_4$ Spinel Nanoparticles Using *Camellia sinensis* Extract: Optical Bandgap Engineering and Sunlight-driven Photocatalytic Wastewater Remediation, *J. Environ. Nanotechnol.*, 15(2), 73–89 (2026). https://doi.org/10.13074/jent.2026.06.2612103

Niksefat, M., Bagheri, R. and Pourjavadi, A., Biodegradable PBAT films with in situ synthesized tannic acid/ZnS nanohybrids for active packaging, offering antioxidant, antibacterial, and UV-shielding properties, *Sci. Rep.*, 16(1), 1198 (2026). https://doi.org/10.1038/s41598-025-30768-x

Panda, B., Lenka, A., Dash, S. K., Panda, R., Naik, K. K., Phaomei, G. and Tripathy, S. K., Biosynthesis and characterization of sheet-like δ-MnO_2 nanomaterials for catalytic degradation of methylene blue and hydrogen peroxide in water, *Mater. Chem. Phy.*, 345, 131236 (2025). https://doi.org/10.1016/j.matchemphys.2025.131236

Rahmani, S., Karimi, R. and Ghorbani, M., Eco-friendly and Green Synthesis of Antibacterial Silver-Nanocomposite Hydrogels with Ultra-High Mechanical Properties, *J. Polym. Environ.*, 33(8), 3749–3771 (2025). https://doi.org/10.1007/s10924-025-03615-3

Revathi, N., Sankarganesh, M., Dhaveethu Raja, J., Rajakanna, J. and Senthilkumar, O., Green synthesis of Plectranthus amboinicus leaf extract incorporated fine-tuned manganese dioxide nanoparticles: Antimicrobial and antioxidant activity, *Inorg. Chem. Commun.*, 154, 110935 (2023). https://doi.org/10.1016/j.inoche.2023.110935

Sharmiladevi, S., Ramesh, N., Prabhu, S. V and Mayakannan, S., Microwave-assisted functionalized biosorbent preparation using seed gum of Tamarindus indica: characterization and evaluation of Cr(VI) removal potency from tannery effluents, *Biomass Convers. Biorefine.*, 14(12), 13533–13545 (2024). https://doi.org/10.1007/s13399-024-05667-2

Shi, Y., Wang, D., Wang, X. and Meng, Z., Hierarchical MnO_2-ZnO functionalized SiO_2 nanofibrous membranes with enhanced Fenton-like catalytic performance for dye removal, *J. Environ. Chem. Eng.*, 11(6), 111618 (2023). https://doi.org/10.1016/j.jece.2023.111618

Suo, H., Yang, Z.-R., Du, K., Fan, J.-W., Dong, E., Xu, Y., Zhang, M., Zhou, N., Yang, L., Jiang, H., Zhu, J. and Tao, J., Pathological-microenvironment responsive injectable GelMA hydrogel with visualized biodegradation for pressure-assisted treatment of hypertrophic scars, *Int. J. Bio. Macromol.*, 292, 139175 (2025). https://doi.org/10.1016/j.ijbiomac.2024.139175

Tang, P., Huang, W., Wang, D., Liu, Z. and Wang, J., 2D Layered K-Birnessite MnO_2-Based Photocatalytic Membrane for Catalytic Filtration Degradation of Organic Pollutants, *Water, Air Soil Pollut.*, 234(2), 120 (2023). https://doi.org/10.1007/s11270-023-06133-x

Thilaga, S. D., Muniyalakshmi, M., Sarika, R., Silambarasan, D. and Prasanna, V. V., Investigation of MnO_2/MWCNTs nanocomposite for various applications, *Next Mater.*, 6, 100475 (2025). https://doi.org/10.1016/j.nxmate.2024.100475

Tiwari, H., Sharma, A. K., Bharti, P. and Agrawal, G., CuO-integrated hydrogel network of gelatin and gellan gum for the efficient sequestration of rhodamine B and crystal violet, *Int. J. Bio. Macromol.*, 320, 146016 (2025). https://doi.org/10.1016/j.ijbiomac.2025.146016

Triadisti, N. and Zamzani, I., Column Chromatography Fractionation and Antioxidant Activity of *Passiflora foetida* Leaves, *Borneo J. Pharm.*, 6(1), 22–30 (2023). https://doi.org/10.33084/bjop.v6i1.1830

Zhang, M., Chen, M., Zhang, L., Li, H., Xiong, E., Wang, S., Wang, Y. and Wang, Z., Internal–external dual cross-linked alginate/gelatin composite hydrogel beads: Structure and pH-responsive gastrointestinal delivery of bioactives, *Food Chem.*, 521, 149841 (2026). https://doi.org/10.1016/j.foodchem.2026.149841